

RESEARCH

Open Access



# Hyperspectral imaging solutions for the non-invasive detection and automated mapping of copper trihydroxychlorides in ancient bronze

Florence Liggins<sup>1</sup>, Alessandra Vichi<sup>1</sup>, Wei Liu<sup>2,3</sup>, Alexander Hogg<sup>1</sup>, Sotiria Kogou<sup>1</sup>, Jianli Chen<sup>3</sup> and Haida Liang<sup>1\*</sup>

## Abstract

Ancient bronze is subject to complex degradation which can lead, in cases where copper chlorides are present, to a cyclic and self-sustaining degradation process commonly referred to as “bronze disease”. If left untreated, bronze disease can eat away at a bronze object until it is entirely deteriorated. The presence of copper trihydroxychlorides is indicative that this process is underway and therefore the detection of these corrosion products is necessary in guiding conservation of ancient bronze artefacts. In this paper we present a high spatial/spectral resolution short wave infrared (SWIR) imaging solution for mapping copper trihydroxychlorides in ancient bronze, combining hyperspectral imaging with an in-house developed unsupervised machine learning algorithm for automated spectral clustering. For this work, verification was obtained through use of an in-house developed reference database of typical ancient bronze corrosion products from several archaeological sites, and from collections of the National Museum of China. This paper also explores the suitability, and limitations, of a visible to near-infrared (VNIR) hyperspectral imaging system as a more accessible solution for mapping copper trihydroxychlorides associated with bronze disease. We suggest that our hyperspectral imaging solution can provide a non-invasive, rapid, and high resolution material mapping within and across bronze objects, particularly beneficial for analysing large collections in a museum setting.

**Keywords:** Reflectance imaging spectroscopy, Hyperspectral imaging, Bronze corrosion, Bronze disease, Automated material mapping

## Introduction

Studies into the chemical composition and metallurgical properties of bronze objects and their patinas and corrosion products have been undertaken for over a century and are still ongoing due to the complex nature of copper and copper-based objects and the very variable environments in which they may have spent the duration

of their existence. The degradation of such artefacts is determined by a chemical interaction of the bronze alloy with the reactive species present in the surrounding environment [1–9]. The effect of the environment upon the degradation can materialise in the form of copper oxides, tenorite CuO and the relatively stable and commonly observed cuprite Cu<sub>2</sub>O; as basic copper carbonates malachite [Cu<sub>2</sub>CO<sub>3</sub>(OH)<sub>2</sub>] and azurite [Cu<sub>2</sub>(CO<sub>3</sub>)<sub>2</sub>(OH)<sub>2</sub>] typically found in a burial environment, or less commonly in sea water or water-logged soil, where there may be a relatively high abundance of CO<sub>2</sub>; as copper chlorides where chlorine from soil or water presents itself as a corrosive agent, or, for outdoor bronzes, as sulfates, such

\*Correspondence: haida.liang@ntu.ac.uk

<sup>1</sup> ISAAC Laboratory, School of Science and Technology, Nottingham Trent University, Nottingham, UK  
Full list of author information is available at the end of the article

as brochantite [ $\text{Cu}_4\text{SO}_4(\text{OH})_6$ ], and antlerite [ $\text{Cu}_3\text{SO}_4(\text{OH})_4$ ], particularly in urban areas due to the presence of sulphuric air pollutants. For a comprehensive review of the subject see Scott et al. [10].

Of these degradation products the ones considered to be most dangerous are the copper chlorides which, when combined with moisture and oxygen, can induce a cyclic and self-sustaining degradation process commonly referred to as 'Bronze Disease'.<sup>1</sup> This process begins with the presence of cuprous chloride ( $\text{CuCl}$ ) known as nanokite, a product of a reaction between cuprous ions and surrounding chloride ions. Cuprous chloride, sparingly soluble in water [14] will, upon being excavated, find itself in favourable conditions for oxidation and hydrolysis creating hydrochloric acid which eats away at uncorroded copper alloy and accelerates the further production of cuprous chloride. In turn, a runaway phenomenon takes place in which the copper trihydroxychlorides, atacamite, clinoatacamite and botallackite, and the more complex polyanionic mineral paratacamite are produced [6].

Identification of the copper trihydroxychlorides, as indicators of the presence of bronze disease, is paramount in considering the preservation of archaeological bronze and in guiding the best approach to an object's conservation, the research into which is itself ongoing [11–15]. This identification is most commonly done either by way of invasive techniques which require sampling an area of interest for analysis or by non-invasive techniques which involve analysis of a localised area. These can include the use of scanning electron microscopes equipped with energy dispersive X-ray spectrometry (SEM-EDS or SEM-EDX), X-ray diffraction (XRD), X-ray fluorescence (XRF) as well as Raman and Fourier Transform Infrared (FTIR) spectroscopy. Due to the necessity of sampling and/or the very localised nature of point-based analyses, the representativeness of data provided by such techniques can often be called into question.

The complexity of bronze patination and the sparsely distributed nature of copper alloy corrosion, mean that it is preferable, particularly in a museum setting where collections of numerous large objects are stored, to develop a method which allows a rapid mapping of material distribution. The use of fibre optics reflectance spectroscopy (FORS) has been tested as a means to effectively and non-invasively identify atacamite and other typical bronze corrosion products [16] with potentialities of the use of the short wave infrared (SWIR) regime in characterising bronze patinas having previously been highlighted

[17]. A more portable miniaturised spectrometer has also been developed for the range 1208–2160 nm in the SWIR and has been demonstrated to be used for, amongst other applications, identifying corrosion on outdoor bronze [19]. Given that reflectance spectroscopy can identify corrosion products effectively on a small scale (limited by the spot size of the fibre optics), the use of spectral imaging would therefore provide a more desirable option for mapping corrosion on a larger scale and at higher spatial resolution. This would also require statistical analysis with a level of automation necessary in processing potentially large high dimensional datasets in an efficient way.

Spectral imaging in the SWIR has been used by Catelli et al. [20] to demonstrate the mapping of sulfates such as antlerite and brochantite on an outdoor bronze sculpture using singular value decomposition (SVD), iterative key set factor analysis (IKSFA) to find the eigen values and 'pure' spectra and the spectral angle mapper (SAM) algorithm to map the corrosion products using a reference spectral database. The SWIR system was placed on a motorised translation stage at a distance of 30 cm, giving a spatial resolution of a few hundred microns. An improved system with higher spatial resolution and ability to scan larger areas would allow a more accurate and efficient mapping of bronze corrosion.

Mapping of bronzes presenting basic copper hydroxysulphate, treated with different organic coatings, has also been achieved by Sciutto et al. [21] using macroscopic FTIR spectroscopy (Alpha, Bruker), in the range 7500–375  $\text{cm}^{-1}$ , and a clustering based data-reduction. The system takes point scans which have been mapped using a motorised 3D stage, which provides scans with spatial resolution limited by the spot size of the instrument.

Remote imaging in the SWIR regime with a large field of view could provide a more practical and effective method for rapid imaging of large bronze objects. We present a high spatial/spectral resolution short wave infrared (SWIR) imaging solution for mapping copper trihydroxychlorides in ancient bronze, combining hyperspectral imaging data with an in-house developed unsupervised machine learning algorithm for automated spectral clustering.<sup>2</sup> Using the same clustering algorithm, we also test the suitability of a visible to near-infrared (VNIR) hyperspectral imaging system as a more affordable solution for mapping bronze disease.

## Methods and materials

### Bronze samples

A number of powdered and fragmented bronze samples from the National Museum of China and School of

<sup>1</sup> So called due to its patches of deterioration which can emerge from below the surface as a green powdery substance and which, if left to continue, can lead ultimately to the degradation of the entire object into a pile of green powder [10].

<sup>2</sup> By spectral clustering we mean clustering pixels with similar reflectance spectra, but not the 'spectral clustering technique' based on graph theory.

Archaeology and Museology, Peking University, Beijing were analysed. Two of the bronze fragments in particular (YJS-M109-19, SJL-M102-8) of around 3–4 cm in size were selected for imaging in this case and are examples of excavated ancient Chinese bronze. They were chosen due to their range in patination over a small surface area and for inclusion of green-blue hues, typical of both stable (e.g. malachite, azurite) and unstable (e.g. atacamite) copper alloy degradation. The fragment from the bronze Yang (YJS-M109-19) was excavated from Yejiashan cemetery, in Suizhou city, Hubei province, dated to the Western Zhou dynasty (1046–771 B.C.), and the other fragment from the bronze Ding vessel (SJL-M102-8) was excavated from Sujialong cemetery, in Jingshan county, Hubei province, dated to the Eastern Zhou dynasty (770–256 B.C.).

### Reference database

Scanning electron microscopy equipped with energy dispersive x-ray analysis (SEM-EDX), X-ray diffraction (XRD), X-ray fluorescence (XRF), Raman spectroscopy, attenuated total reflection Fourier transform infrared (ATR-FTIR) spectroscopy and FORS analyses were carried out on the powdered samples of Chinese bronze (see section *Bronze Samples*) in order to build a small reference database of typical corrosion products on bronzes from several archaeological sites including Yejiashan, Panlongcheng, Sujialong sites in Hubei province, Beizhen site in Liaoning province, and collections of the National Museum of China. FORS measurements were acquired using an ASD LabSpec spectrometer, covering the range 350 nm to 2500 nm with spectral resolution of 3 nm and 10 nm in the VNIR and SWIR respectively. The XRD data were acquired using Rigaku-D/max-rB and Rigaku-DMAX 2200 equipped with a Cu K $\alpha$  source, in the  $2\theta$  range 3°–70° and 10°–70°. The voltage and current were set at 40 kV and 40 mA respectively. Raman analysis was carried out using Renishaw inVia Raman spectrometer with air cooled DPSS laser operating at a maximum power of 50 mW at 532 nm. The laser power varied from 0.5 to 5% of the maximum power depending on the sample analysed. The exposure time was 10 s with 2 times accumulation. PHENOM XL Desktop SEM equipped with EDS was used to acquire the elemental components. The acceleration voltage was 15 kV and a low vacuum mode was used. ATR-FTIR spectra were collected with an Agilent Cary 630 spectrometer fitted with a diamond crystal. The spectral range was 4000–400 cm<sup>-1</sup>, and 128 spectra were co-added per sample with an 8 cm<sup>-1</sup> spectral resolution.

The degraded bronze samples analysed and used for reference are listed in Table 1 giving the sample number, name of the object from which the sample was taken, the

period of the object, the site from which it was found, the condition (ground or unground) of the sample, the chemical composition and the analysis methods used. The final column in Table 1 gives the RGB colour, derived from the reflectance spectrum acquired using FORS, assuming a standard D65 daylight illuminant and colour-matching functions for the CIE 1931 2° standard colorimetric observer [22, 23]. What is interesting to note here is that the RGB colour can be very similar for samples with entirely different chemical composition (see ID 2 and 3 in Table 1, for example) whilst the RGB colour of a single sample can also vary greatly depending on whether it is in ground or unground condition (see ID 1 and 2) showing the importance of particle size and sample condition upon the visible colour.

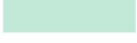
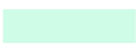
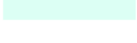
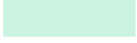
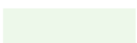
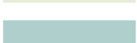
Supplementary to this database, FORS measurements of pigment powders containing atacamite, malachite and azurite were taken, the constituents of which were determined through XRD measurements (see Table 2). The reflectance spectra obtained for these pigments are shown in Fig. 1 for the VNIR (left) and SWIR (right) spectral regions, and were also used as reference. It is shown from these, the clear difference in spectral features observed for pigments containing each of the three copper degradation products, and therefore the possibility to distinguish between them, not only in the SWIR but also the VNIR.

To our knowledge, there is little in the literature on reflectance spectroscopic data for atacamite [16, 17, 26], and none for clinoatacamite, in the SWIR region of the spectrum.<sup>3</sup> We therefore include here the measured spectra of atacamite and clinoatacamite (see Fig. 2), and the corresponding observed absorption features in the SWIR are also given in Table 3. We find that the characteristic spectral features of atacamite as measured for this work match those given by Catelli et al. [17] in their distinction of atacamite and non-zincian paratacamite in the region 7500–4000 cm<sup>-1</sup> (corresponding to 1333–2500 nm). These measurements are given in Table 3 and were also used as reference. Interestingly we also found that many of the absorption features which we assigned to clinoatacamite, also match those assigned to paratacamite in Catelli et al. [17], therefore, it appears that clinoatacamite and paratacamite have similar spectra in this region. It is worth noting that these similarities were also observed in the spectral range 4000–400 cm<sup>-1</sup>.

Overall the reference datasets obtained for our analysis represent both naturally occurring bronze degradation products in ground and unground condition, and natural

<sup>3</sup> This is despite the interest in these materials as pigments in Asia [26], South America, Egypt and Europe [18].

**Table 1** Degraded ancient Chinese bronze samples

ID	Sample no.	Object	Period	Site	Condition	Chemical composition	Analysis methods	Derived RGB colour
1	YJS-126-18-1	Bronze Zun vessel	Western Zhou (西周)	Yejiashan, Hubei	Ground	Cuprite, Malachite	XRD, SEM-EDS, ATR-FTIR, FORS	
2	YJS-126-18-1	Bronze Zun vessel	Western Zhou (西周)	Yejiashan, Hubei	Unground	Cuprite, Malachite	XRD, SEM-EDS, FORS	
3	LN-BZ-93	Bronze Mirror	Liao Dynasty (辽代)	Beizhen, Liaoning	Ground	Atacamite, Clinoatacamite, Quartz	XRD, SEM-EDS, ATR-FTIR, FORS	
4	LN-BZ-96	Bronze Mirror	Liao Dynasty (辽代)	Beizhen, Liaoning	Ground	Atacamite, Clinoatacamite, Quartz	XRD, SEM-EDS, FORS	
5	LN-BZ-113	Bronze Mirror	Liao/Jin (辽/金)	Beizhen, Liaoning	Ground	Atacamite, Clinoatacamite, Quartz	XRD, SEM-EDS, FORS	
6	LN-BZ-151-1	Bronze Mirror	Jin Dynasty (金)	Beizhen, Liaoning	Ground	Atacamite, Clinoatacamite, Quartz	XRD, SEM-EDS, ATR-FTIR, FORS	
7	SJL-M82-1	Bronze Ding vessel	Spring and Autumn (春秋)	Sujialong, Hubei	Unground	Clinoatacamite, Cuprite, Atacamite	XRD, SEM-EDS, ATR-FTIR, FORS, Raman	
8	SJL-M84-7	Bronze Gui vessel	Spring and Autumn (春秋)	Sujialong, Hubei	Unground	Atacamite, Clinoatacamite	XRD, SEM-EDS, ATR-FTIR, FORS	
9	SJL-M102-11	Bronze Li vessel	Spring and Autumn (春秋)	Sujialong, Hubei	Unground	Clinoatacamite, Quartz	XRD, SEM-EDS, ATR-FTIR, FORS	
10	PLC-27	Bronze Ding vessel	Shang Dynasty (商代)	Panlongcheng, Hubei	Ground	Cassiterite	XRD, SEM-EDS, ATR-FTIR, FORS	
11	PLC-27	Bronze Ding vessel	Shang Dynasty (商代)	Panlongcheng, Hubei	Unground	Cassiterite	XRD, SEM-EDS, FORS	
12	PLC-9	Bronze Ding vessel	Shang Dynasty (商代)	Panlongcheng, Hubei	Ground	Cassiterite, Romarchite, Cuprite	XRD, SEM-EDS, ATR-FTIR, FORS, Raman	
13	PLC-9	Bronze Ding vessel	Shang Dynasty (商代)	Panlongcheng, Hubei	Unground	Cassiterite, Romarchite, Cuprite	XRD, SEM-EDS, FORS, Raman	
14	PLC-36	Bronze Jia vessel	Shang Dynasty (商代)	Panlongcheng, Hubei	Ground	Cassiterite, Romarchite, Cuprite	XRD, SEM-EDS, ATR-FTIR, FORS, Raman	
15	PLC-36	Bronze Jia vessel	Shang Dynasty (商代)	Panlongcheng, Hubei	Unground	Cassiterite, Romarchite, Cuprite	XRD, SEM-EDS, FORS, Raman	
16	YJS-B-M111-58-3	Bronze Gui vessel	Western Zhou (西周)	Yejiashan, Hubei	Unground	Azurite	SEM-EDS, ATR-FTIR, FORS, Raman	
17	OFY-8	Bronze 'Fuhao' double square Yi vessel	Shang Dynasty (商代)	National Museum of China, Beijing	Unground	Sampleite, Malachite	XRD, SEM-EDS, ATR-FTIR, FORS, Raman	

and synthetic mineral pigments with azurite, malachite and atacamite as their main components.

### Spectral imaging

Spectral imaging data were acquired in both the short-wave infrared (930–2500 nm) and the visible to near-infrared (400–1000 nm) regimes using an adapted commercial system and an in-house built system respectively.

### SWIR

Hyperspectral images in the shortwave infrared were acquired using a HySpex SWIR-384 hyperspectral camera from NEO operating in the range 930–2500 nm with a spectral resolution of 5.45 nm and a total of 288 channels. This instrument adopts a line-scan (or ‘pushbroom’) mechanism providing 384 spatial pixels from a 16 bit cooled HgCdTe (MCT) sensor. The optics of the HySpex SWIR-384 imaging system was adapted in order to improve the spatial resolution, and includes the use of a Meade ETX-90 telescope with a focal length of 1250 mm and an aperture diameter of 90 mm. This allows remote sensing in the SWIR with a spatial resolution of around 125  $\mu\text{m}$  at 3.5 m distance. A system is mounted upon an alt-az telescope mount which allows rapid imaging of large objects or multiple objects at a time by scanning via computer control. This is particularly useful for imaging of museum objects, including large objects or sites, at short- to long-range distances. Calibration of the spectra was achieved using a 5"  $\times$  5" 99% Spectralon<sup>®</sup> diffuse reflectance target.

### VNIR

Hyperspectral images in the visible to near-infrared regime were acquired using an in-house line-scan imaging system developed at the ISAAC laboratory, Nottingham Trent University. The system consists of an Andor Technology Ltd. Zyla sCMOS camera combined with a Specim ImSpector V10E spectrograph operating in the range 400–1000 nm. The spectrograph provides a spectral resolution of 2.8 nm (with 30  $\mu\text{m}$  slit) and after rebinning gives a total of 132 channels with sampling resolution of 4.53 nm. A Meade ETX90 telescope was attached to the spectrograph and camera system, in addition to an automated focussing mechanism, which allows fully focused, high resolution spectral images of 3-dimensional objects to be obtained. The acquired VNIR data were processed to output both a 3-dimensional spectral image cube and a colour RGB image, derived from the VNIR image cube assuming a standard D65 daylight illuminant and CIE 1931 2° standard colorimetric observer [22, 23]. Calibration of the spectra was achieved using a 99% Spectralon<sup>®</sup> diffuse reflectance target. For this

work, the first 4 channels were removed because of their low signal to noise ratio, and the 20th channel was also replaced with an interpolated image due to an artefact caused by the order sorting filter, leaving a total of 128 spectral bands.

### Automated material mapping

The clustering code for grouping similar reflectance spectra used for this work is an in-house developed, python-based, unsupervised machine learning code which employs an adaptation of Kohonen’s ‘self organising map’ (SOM) [24, 25] and is based on a code similar to that described in Kogou et al. [26]. The benefits of SOM, in comparison to other spectral clustering algorithms, for analysing large datasets with high dimensional spectra has been previously outlined [26, 27]. The code used for this work requires minimal user input and does not require a labelled training set.

A SOM is a map consisting of a number of neurons, or nodes, to which initial weight vectors are randomly assigned and given the same length as your input vectors. For the case of a spectral imaging dataset, the input vectors are spectra, with length defined by the number of spectral bands. When applying SOM to the dataset, each input spectrum is compared with weight vectors, or representative spectra, of each node in the map in order to find its ‘winning neuron’, where the calculated Euclidean distance between input and weight vectors are found to be minimum. Weight vectors which lie within the neighbourhood of the winning neuron are then activated by one another, learning from the input spectrum which in turn results in a re-evaluation of weights, pulling nodes in this defined neighbourhood closer to the input spectrum. This learning can be described by the equation

$$w_v(s+1) = w_v(t) + \alpha(s)\theta(u, v, s)[X(t) - w_v(s)] \quad (1)$$

where  $s$  is the current iteration step,  $v$  is the node index,  $u$  is the index of the best matching weight on the map,  $w$  is the weight vector,  $\alpha$  is the learning rate,  $\theta$  is the smoothing kernel used, or neighbourhood function,  $X(t)$  is the input spectrum from dataset  $X$  (all data from your image cube), and  $t = 0, 1, \dots, N$  where  $N$  is the total number of pixels in the dataset. This process is known as a ‘winner takes all’ learning process at the end of which data are described as being a member of a cluster at a given node. A measure of how close the final weight,  $W_j$ , at this node is, for a given cluster  $j$ , to the input spectra,  $x_{ij}$ , can be described by the quantization error, and is given by

$$QE_j = \frac{1}{n} \sum_{i=0}^n |x_{ij} - W_j| \quad (2)$$

**Table 2** Reference pigment powders

Pigment name	Formation	Company	XRD Result
Azurite (Kremer)	Natural	Kremer	Azurite 67% malachite 14% quartz 15% Muscovite 4%
Azurite (Tianya)	Natural	天雅 Tianya	Azurite 94% malachite 2% cuprite 2% quartz 2%
Malachite (Kremer)	Synthetic	Kremer	Malachite 100%
Malachite (Tianya)	Natural	天雅 Tianya Mineral & Pigment	Malachite 100%
Malachite (Sinopharm)	Synthetic	国药试剂 Sinopharm Chemical Reagent	Malachite 100%
Cu <sub>2</sub> (OH) <sub>3</sub> Cl (Buddha 317)	Natural	Sample Buddha 317 [16]	Atacamite 46%, clinoatacamite 54%
Cu <sub>2</sub> (OH) <sub>3</sub> Cl (Xiya)	Synthetic	西亚试剂 Xiya Reagent	Atacamite 33%, paratacamite 28%, clinoatacamite 39%
Atacamite (Kremer)	Natural	Kremer	Atacamite 86%, quartz 14% *

\* Kaolin also detected through use of FTIR spectroscopy

where  $n$  is the number of input spectra assigned to the given ( $j$ th) cluster, and  $|x_{ij} - W_j|$  is the absolute distance between the input spectra and final weight.

For each spectral region (SWIR, VNIR), all spectral data are extracted from the image cube and the clustering code is then applied, in order to automatically group the spectra into distinct clusters. Firstly, the data are clustered using SOM in order to reduce the dimensionality of the data and the mean spectrum for each cluster is calculated. These reduced data, consisting of mean spectra for each distinct cluster, are then normalised, and a secondary clustering is applied, again using SOM. The normalisation of the spectra, in this case, allows us to group by spectral shape without giving significance to absolute reflectance. To assess the quality of each cluster, the quantization error, Q.E., is calculated and for clusters whose quantization error falls outside of a designated threshold, the cluster is removed and the data retained for reclustering. This process is repeated iteratively, with an incremental increase in the threshold, until all data are assigned a cluster number. Following this, a merging process is carried out, in which clusters are merged if they satisfy the criterion that their mean spectrum falls

within one standard deviation of another cluster's and vice versa. The clusters are mapped back to their original images and each pixel is assigned its cluster number. The resulting output cluster maps show areas which share spectral similarities and are therefore likely to share the same material composition. The mean spectrum for each cluster is also provided which can then be used to compare with a reference database for preliminary material identification. For the purpose of this work, single image cubes (SWIR and VNIR) were analysed at a time. However, this clustering technique can be applied to multiple spectral image cubes simultaneously, allowing materials to be mapped within and across objects, which would be beneficial for the analyses of museum collections.

## Results and discussion

### SWIR analysis

For the detection and mapping of copper trihydroxychlorides associated with bronze disease, and in order to test whether we are able to distinguish these from other less harmful, but similar hued, bronze corrosion products, the large bronze samples were imaged in the SWIR and

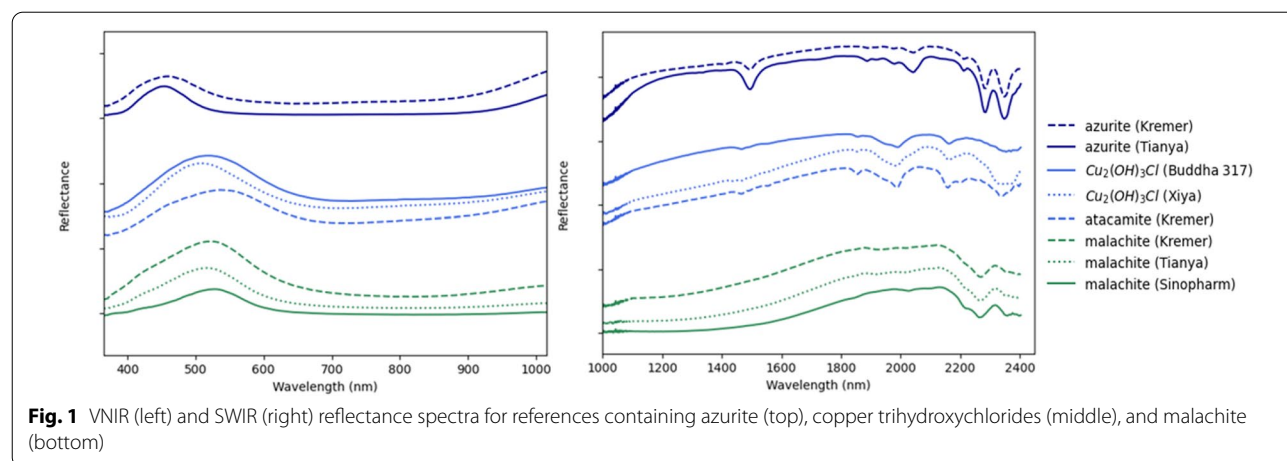


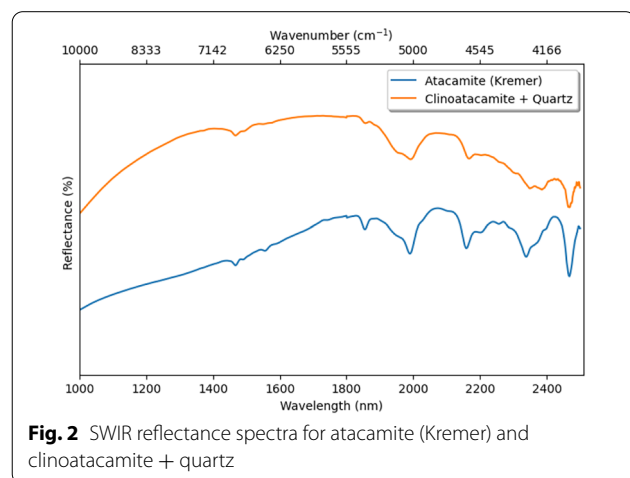
**Table 3** Wavelengths and wavenumbers for observed spectral features in the SWIR region for copper trihydroxychlorides atacamite (Kremer) and clinoatacamite

Atacamite (nm) [17]	Atacamite (cm <sup>-1</sup> ) [17]	Atacamite (nm) (this work)	Atacamite (cm <sup>-1</sup> ) (this work)	Clinoatacamite+quartz (nm) (this work)	Clinoatacamite+quartz (cm <sup>-1</sup> ) (this work)
2467	4053	2467	4053	2386	4191
				2351	4253
2342	4270	2339	4275		
2260	4424	2259	4426		
2161	4627	2160	4630	2166	4616
				1996	5010
1191	5023	1990	5024		
1856	5388	1855	5390	1856	5387
1467	6818	1466	6820	1466	6820

spectral clustering applied using our automated unsupervised clustering code. The full spectral data were then recovered in order to calculate the mean spectrum for each unique cluster as part of the post-processing. The output gives a cluster map, with each pixel assigned a cluster number. In addition, single cluster maps are given for each cluster by masking and retaining the original colour or false colour image for pixels associated with that cluster. Clusters and cluster maps can be combined where the user finds it appropriate based on the signatures detected, for example, where only the spectral features are important but the variation in intensity holds little importance.

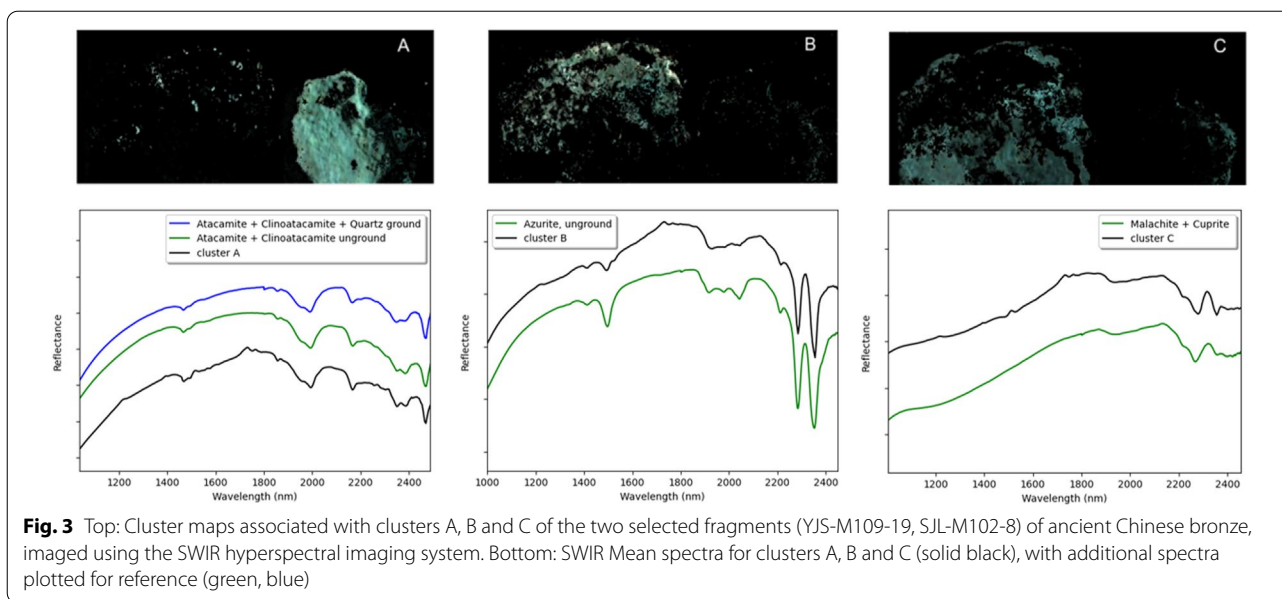
For the ancient bronze samples imaged, we found areas corresponding to three significant spectral signatures which are mapped as A, B, and C in Fig. 3 (top). By visual observations of the colour image alone (see RGB image in Fig. 4), it is not obvious where these areas lie, nor whether we would be able to distinguish them as chemically different from one another. The single cluster maps

were used as a mask for the original spectral image cube in order to obtain spectra corresponding to a single given cluster. Clusters A, B and C were then identified using the reference database which was in turn verified with multimodal spectral analysis (see Table 1). The resulting mean spectra for each cluster A, B and C can be seen in Fig. 3 (bottom) with reference reflectance spectra over-plotted. Importantly we detected and mapped the copper trihydroxychlorides atacamite and clinoatacamite, associated with bronze disease, for cluster A. Quartz grains can often be found on excavated ancient bronze and are connected to soil contamination in the burial environment [5, 10, 28], however their presence is not well determined using reflectance data alone, given that the quartz reflectance is largely featureless due to its transparency. Cluster B was identified as areas containing azurite, and cluster C can be identified as a malachite and cuprite mix. The identification of these areas could not be done with good accuracy using pure or synthesised compounds as reference, which reinforces the importance of producing and maintaining an in-house database, based on real archaeological samples, for the analysis of ancient bronze objects.



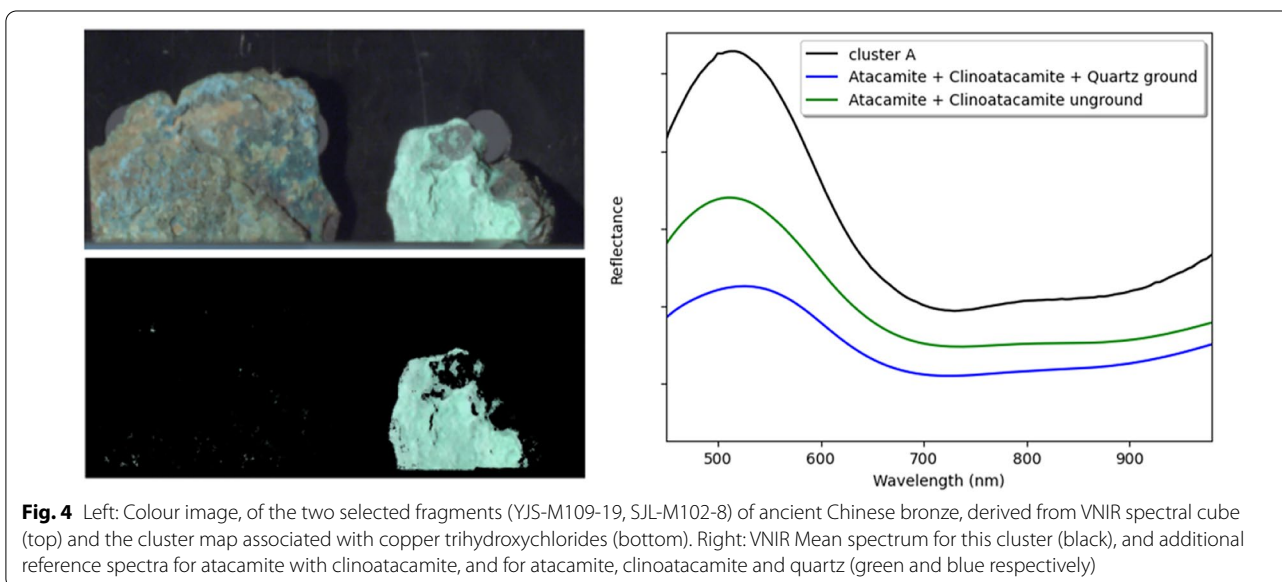
### VNIR analysis

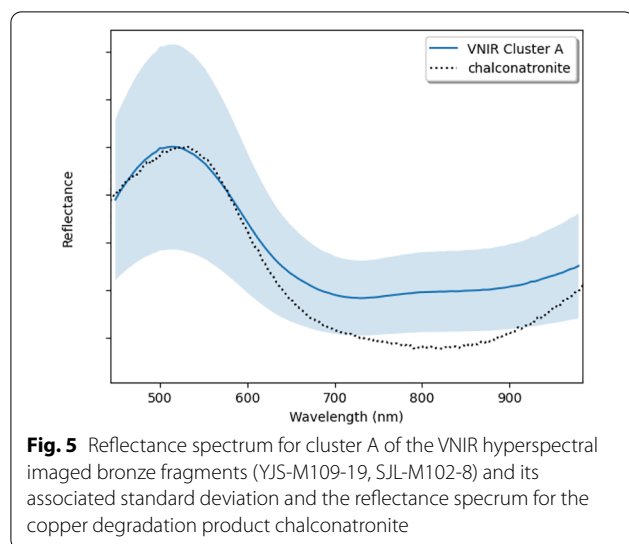
The use of the VNIR reflectance spectroscopy in the detection or identification of bronze disease has been largely unexplored, due to the broad spectral features of copper-based compounds in this spectral region. Results from FORS measurements, however, show that, in principle, the copper trihydroxychlorides should be distinguishable from the commonly observed and more stable malachite and azurite (see Fig. 1). For this work, the same samples imaged by the SWIR spectral imaging instrument were also imaged using the VNIR spectral camera. Following this, the spectral clustering was applied to



the VNIR spectral image cube in order to see if we can detect and map the same copper trihydroxychlorides as in the previous SWIR analysis. The resulting cluster map showed that indeed the areas containing atacamite and clinoatacamite could be distinguished from the other bronze degradation products present. The colour image derived from the VNIR spectral image cube can be seen in Fig. 4 along with the cluster map associated with the mix of copper trihydroxychlorides, atacamite and clinoatacamite. The mean spectrum for the cluster is also shown in Fig. 4 (right) to be consistent in spectral shape with the reference spectra for atacamite with

clinoatacamite. The peak at around 512 nm, as well as the two absorption bands at around 720 nm and 895 nm, appears to correspond to that of the copper trihydroxychloride mix of atacamite and clinoatacamite. The cluster map agrees with Cluster A from the SWIR analysis. It should be noted that it is not advisable to attempt identification of the copper trihydroxychlorides using VNIR reflectance spectral imaging analysis alone, but such an analysis is sufficient to map areas of similar material composition, which can then be followed up with complementary non-invasive point analysis methods for verification (e.g. FORS measurements covering the SWIR).





Although we were successful in detecting and mapping the copper trihydroxychlorides in this case, it must be noted that reflectance spectra in this region are sensitive to the particle size, particularly for some copper-based pigments and degradation products [29, 30], and although the identification of copper-based pigments in this region is done by each of their characteristic absorption features, the resulting ‘peak’ between two absorption bands, can indeed shift and broaden depending on the particle size of the product in question. Such a shift may be problematic for identification where more degradation products are involved. The bronze degradation product chalconatronite, sodium-copper carbonate, has also previously been found to share spectral similarities in the VNIR to the copper trihydroxychlorides, whilst exhibiting clearly distinct spectral features in the SWIR [16]. Figure 5 shows the reflectance spectrum of chalconatronite in the (black) with the mean reflectance spectrum of Cluster A from our VNIR analysis, associated with the atacamite and clinoatacamite mix present in the bronze samples. The standard deviation associated with the mean spectrum for Cluster A is also plotted. We can see from this figure that in this case, the spectrum of chalconatronite does not fall within one standard deviation of the cluster mean, and therefore if it were present in the imaged bronze samples, it is possible that it would be distinguished from the copper trihydroxychlorides and assigned its unique cluster. The clustering algorithm, however, would also take into consideration the standard deviation of the mean spectrum for the chalconatronite cluster, which would in turn be dependent on the number of pixels containing chalconatronite spectra. With these limitations in mind, it is recommended that the VNIR spectral imaging solution therefore be used with caution, and suggested that this spectral region be investigated further.

## Conclusions

In the SWIR regime, using a high spatial and spectral resolution imaging system, combined with an in-house developed machine learning-based spectral clustering code, we have been able to rapidly detect and identify copper trihydroxychlorides, responsible for bronze disease, in ancient bronze, and we have also been able to easily map and distinguish between stable (e.g. malachite, azurite) and unstable (e.g. atacamite, clinoatacamite) copper-based corrosion products, typically found in ancient bronze collections. This SWIR spectral imaging system would be ideal for rapid detection and mapping of copper trihydroxychlorides on multiple bronze objects within a collection or for the scanning of large objects. It has advantage over invasive methods involving sampling and/or non-invasive point analyses which are time consuming and do not provide fully representative data. The identification of the copper trihydroxychlorides, indicative of the presence of bronze disease, is achievable through use of an in-house reflectance spectral database made specifically for the bronze collection at the National Museum of China, Beijing, to test the applicability of the system. The database provides more accurate identification where mixtures are involved.

This process was repeated for a VNIR hyperspectral imaging system, using the same spectral clustering code. The copper trihydroxychlorides were again able to be mapped as verified by the original SWIR data as well as the in-house database for ancient bronze samples. This spectral imaging system, combined with the automated spectral clustering, enables the mapping of spectral differences (and therefore different material composition), which can then be followed up with non-invasive point-based analysis (e.g. FORS covering the SWIR region) as a more accessible or financially viable solution to mapping bronze disease. It is, however, advised that the SWIR spectral imaging solution is the preferred method for mapping copper trihydroxychlorides owing to the sharp characteristic absorption bands in the SWIR range. The drawbacks of VNIR hyperspectral imaging are the dependency of particle size upon the shift of the observed reflectance ‘peak’ in the VNIR spectral region for some copper-based corrosion products, and the potential challenges in distinguishing between copper trihydroxychlorides and chalconatronites (not present in our imaged samples) whose VNIR spectra are similar.

Our results show that hyperspectral imaging, combined with automated spectral clustering, can provide a means to map and identify copper trihydroxychlorides, and therefore bronze disease, to more rapidly and effectively guide further analyses for the conservation of ancient bronze objects. These spectral imaging solutions are not limited to the detection of corrosion indicative

of the presence of bronze disease, but could also provide a means to map other forms of patination and bronze corrosion (e.g. sulfates for outdoor bronzes) over time in order to monitor, spectrally and spatially, the condition evolution of a bronze object, or collection of bronze objects, of interest.

#### Abbreviations

ATR: Attenuated total reflectance; FTIR: Fourier Transform Infrared; FORS: Fibre optics reflectance spectroscopy; ISAAC: Imaging & Sensing for Archaeology, Art History & Conservation; SEM-EDS/SEM-EDX: Scanning electron microscopes equipped with energy dispersive X-ray spectrometry; SWIR: Short wave infrared; VNIR: Visible to near-infrared; XRD: X-ray diffraction; XRF: X-ray fluorescence.

#### Acknowledgements

We thank Luke Butler for his help in VNIR hyperspectral data acquisition.

#### Author contributions

Conceptualisation: HL, WL; Formal analysis: FL, WL, AV; Funding acquisition: HL; Investigation: FL, WL, AV; Resources: AH, SK, WL, JC; Software: FL; Supervision: HL, JC; Writing-original draft: FL; Writing-review and editing: HL, AV, WL. All authors read and approved the final manuscript.

#### Funding

Funding from UK Natural Environment Research Council (NERC) Grant NE/R014868/1, UK Arts and Humanities Research Council (AHRC) Grant AH/T013184/1 and Nottingham Trent University are gratefully acknowledged.

#### Availability of data and materials

The datasets used and/or analysed during the current study are available from the corresponding author on reasonable request.

#### Declarations

##### Competing interests

The authors declare that they have no competing interests.

##### Author details

<sup>1</sup>ISAAC Laboratory, School of Science and Technology, Nottingham Trent University, Nottingham, UK. <sup>2</sup>The National Museum of China, Beijing, Dongcheng, China. <sup>3</sup>School of Archaeology and Museology, Peking University, Beijing, Haidian, China.

Received: 24 June 2022 Accepted: 30 July 2022

Published online: 09 September 2022

#### References

- Robbiola L, Blengino JM, Fiaud C. Morphology and mechanisms of formation of natural patinas on archaeological Cu-Sn alloys. *Corros Sci*. 1998;40(12):2083–111.
- Serghini-Idrissi M, Bernard MC, Harrif FZ, Joiret S, Rahmouni K, Srhiri A, Takenouti H, Vivier V, Ziani M. Electrochemical and spectroscopic characterizations of patinas formed on an archaeological bronze coin. *Elect Acta*. 2005;50(24):4699–709.
- Robbiola L, Rahmouni K, Chiavari C, Martini C, Prandstraller D, Texier A, Takenouti H, Vermaut P. New insight into the nature and properties of pale green surfaces of outdoor bronze monuments. *Appl Phys*. 2008;92(1):161–9.
- Mezzi A, De Caro T, Riccucci C, Faraldi F, Veroli C, Caschera D. Unusual surface degradation products grown on archaeological bronze artefacts. *Appl Phys*. 2013;113(4):1121–8.
- Soffritti C, Fabbri E, Merlin M, Garagnani GL, Monticelli C. On the degradation factors of an archaeological bronze bowl belonging to a private collection. *Appl Surf Sci*. 2014;313:762–70.
- Scott DA. New insights on the corrosion of ancient bronzes using X-ray powder diffraction: The importance of paratacamite, sampleite, and conellite. *Stud Conserv*. 2017;62(7):410–8.
- Oudbashi O, Fadaei H. After Eighty Years: Experimental Study of Atmospheric Corrosion in the Metallic Dome of Hafez's tomb, Shiraz, Iran. *Stud Conserv*. 2019;64(4):208–20.
- Chang T, Maltseva A, Volovitch P, Odnevall Wallinder I, Leygraf C. A mechanistic study of stratified patina evolution on Sn-bronze in chloride-rich atmospheres. *Corros Sci*. 2020;166: 108477.
- Rémazeilles C, Langlet-Marzloff V, Creus J, Lotte G, Deshayes C, Baleux F, Robbiola L. Remarkable corrosion resumption of archaeological bronzes, induced by the oxidation of ternary Cu-Sn-S phases in atmosphere, after long-term burial with sulfides. *Corros Sci*. 2020;175: 108865.
- Scott DA. *Copper and Bronze in Art, Corrosion, Colorants, Conservation*. Malibu: Paul Getty Conservation Institute; 2002.
- Artasani A, Turo F, Di, Zucchelli M, Traviglia A. Recent advances in protective coatings for cultural heritage - an overview. *Coatings*. 2020;10(3):217.
- Albini M, Letardi P, Mathys L, Brambilla L, Schröter J, Junier P, Joseph E. Comparison of a bio-based corrosion inhibitor versus benzotriazole on corroded copper surfaces. *Corros Sci*. 2018;143:84–92.
- Di Francia E, Lahoz R, Neff D, de Caro T, Angelini E, Grassini S. Laser-cleaning effects induced on different types of bronze archaeological corrosion products: chemical-physical surface characterisation. *Appl Surf Sci*. 2022;573: 150884.
- Näsänen L, Kasprzak L, Cretté S, González-Pereyra N, & Watkinson D. Feasibility of Subcritical Fluid Technology to Stabilize Archaeological Copper Alloy Artifacts. In: Menon R, Chemello C, Pandya A eds. *Metal 2016 Proceedings of the Interim Meeting of the ICOM-CC Metals Working Group September 2017; 26-30, 2016 New Delhi India*.
- Petiti C, Toniolo L, Gulotta D, Mariani B, Goidanich S. Effects of cleaning procedures on the long-term corrosion behavior of bronze artifacts of the cultural heritage in outdoor environment. *Environ Sci Pollut Res*. 2020;27(12):13081–94.
- Liu W, Li M, Wu N, Liu S, Chen J. A new application of Fiber optics reflection spectroscopy (FORS): Identification of "bronze disease" induced corrosion products on ancient bronzes. *J Cult Herit*. 2021;49:19–27.
- Catelli E, Sciutto G, Prati S, Jia Y, Mazzeo R. Characterization of outdoor bronze monument patinas: the potentialities of near-infrared spectroscopic analysis. *Environ Sci Poll Res*. 2018;25(25):24379–93.
- Nord AG, Tronner K. The Frequent Occurrence of Atacamite in Medieval Swedish Murals. *Stud Conserv*. 2018;63(8):477–81.
- Catelli E, Sciutto G, Prati S, Lozano MVC, Gatti L, Lugli F, Silvestrini S, Benazzi S, Genorini E, Mazzeo R. A new miniaturised short-wave infrared (SWIR) spectrometer for on-site cultural heritage investigations. *Talanta*. 2020;218: 121112.
- Catelli E, Randeberg LL, Strandberg H, Alsberg BK, Maris A, Vikki L. Can hyperspectral imaging be used to map corrosion products on outdoor bronze sculptures? *J Spectral Imaging*. 2018;7:2040–4565.
- Sciutto G, Legrand S, Catelli E, Prati S, Malegori C, Oliveri P, Janssens K, Mazzeo R. Macroscopic mid-FTIR mapping and clustering-based automated data-reduction: An advanced diagnostic tool for in situ investigations of artworks. *Talanta*. 2020;209:120575–81.
- CIE Colorimetry, 2004. 3rd Ed. CIE Publication 015:2004. Central Bureau of the CIE, Vienna.
- McLaren K. XIII-The Development of the CIE 1976 (L\* a\* b\*) Uniform Colour Space and Colour-difference Formula. *J Soc Dyers Colourists*. 1976;92(9):338–41.
- Kohonen T. The Self-Organizing Map. *Proc IEEE*. 1990;78(9):1464–80.
- Vettigli G. MiniSom: minimalistic and NumPy-based implementation of the Self Organizing Map. 2018; <https://github.com/JustGlowing/minisom/>.
- Kogou S, Shahtahmassebi G, Lucian A, Liang H, Shui B, Zhang W, Su B, van Schaik S. From remote sensing and machine learning to the history of the Silk Road: large scale material identification on wall paintings. *Sci Rep*. 2020;10(1):1–15.
- Kogou S, Lee L, Shahtahmassebi G, Liang H. A new approach to the interpretation of XRF spectral imaging data using neural networks. *X-Ray Spectrometry*. 2021;50:310–9.
- Mahmoud GA, Elserogy AR. Deterioration and conservation of an assyrian bronze kneading bowl. *Shedet*. 2020;7:250–62.

29. Liang H. Advances in multispectral and hyperspectral imaging for archaeology and art conservation. *Appl Phys.* 2012;106(2):309–23.
30. Gueli AM, Bonfiglio G, Pasquale S, Troja SO. Effect of particle size on pigments colour. *Color Res Appl.* 2017;42(2):236–43.

### **Publisher's Note**

Springer Nature remains neutral with regard to jurisdictional claims in published maps and institutional affiliations.

**Submit your manuscript to a SpringerOpen<sup>®</sup> journal and benefit from:**

- ▶ Convenient online submission
- ▶ Rigorous peer review
- ▶ Open access: articles freely available online
- ▶ High visibility within the field
- ▶ Retaining the copyright to your article

---

Submit your next manuscript at ▶ [springeropen.com](https://www.springeropen.com)

---